The Astrophysical Journal, 850:198 (11pp), 2017 December 1 https://doi.org/10.3847/1538-4357/aa9849

The Formation of Super-Earths by Tidally Forced Turbulence

Cong Yu
School of Physics and Astronomy, Sun Yat-Sen University, Guangzhou, 519082, P. R. China; yucong@mail.sysu.edu.cn
Received 2017 August 8; revised 2017 October 14; accepted 2017 November 1; published 2017 December 4

Abstract

The *Kepler* observations indicate that many exoplanets are super-Earths, which brings about a puzzle for the core-accretion scenario. Since observed super-Earths are in the range of critical mass, they accrete gas efficiently and become gas giants. Theoretically, super-Earths are predicted to be rare in the core-accretion framework. To resolve this contradiction, we propose that the tidally forced turbulent diffusion may affect the heat transport inside the planet. Thermal feedback induced by turbulent diffusion is investigated. We find that the tidally forced turbulence generates pseudo-adiabatic regions within radiative zones, which pushes the radiative-convective boundaries inward. This decreases the cooling luminosity and enhances the Kelvin–Helmholtz (KH) timescale. For a given lifetime of protoplanetary disks (PPDs), there exists a critical threshold for the turbulent diffusivity, $\nu_{\rm critical}$. If $\nu_{\rm turb} > \nu_{\rm critical}$, the KH timescale is longer than the disk lifetime and the planet becomes a super-Earth, rather than a gas giant. We find that even a small value of turbulent diffusion has influential effects on the evolution of super-Earths. The $\nu_{\rm critical}$ increases with the core mass. We further ascertain that, within the minimum-mass extrasolar nebula, $\nu_{\rm critical}$ increases with the semimajor axis. This may explain the feature that super-Earths are common in inner PPD regions, while gas giants are common in outer PPD regions. The predicted envelope mass fraction is not fully consistent with observations. We discuss physical processes, such as late core assembly and mass-loss mechanisms, that may be operating during super-Earth formation.

Key words: instabilities – planets and satellites: formation – protoplanetary disks – turbulence – waves

1. Introduction

One of the widely accepted mechanisms of planet formation is the core-nucleated instability theory (Perri & Cameron 1974; Harris 1978; Mizuno et al. 1978; Stevenson 1982). According to this scenario, the massive gaseous atmosphere is accumulated in a runaway manner when the core mass reaches a critical value. In static models, when heating balances cooling, runaway accretion occurs when the planet is beyond the critical mass, because the envelope fails to hold hydrostatic equilibrium. Rafikov (2006) found a broad range of critical mass ($0.1\ M_\oplus \leqslant M_{\rm critical} \leqslant 100\ M_\oplus$) due to various disk properties and planetesimal accretion rates. However, in dynamic or quasi-static models, the thermal disequilibrium rather than the hydrostatic disequilibrium plays the dominant role. The runaway accretion occurs because the envelope becomes thermally unstable as the cooling timescale becomes catastrophically shorter. In this case, the runaway accretion is driven by runaway cooling (Bodenheimer & Pollack 1986; Lee et al. 2014; Piso & Youdin 2014). Three stages are involved in the formation process. In the first stage, rocky cores grow by rapid planetesimal accretion. In the second stage, the core's feeding zone is depleted of solids and the atmosphere grows gradually, regulated by the Kelvin–Helmholtz (KH) contraction. Finally, when the atmosphere reaches the crossover mass, gas runaway takes place, and the planet gets inflated into a gas giant. The timescale of the second stage is the longest among the three and dominates the whole formation process (Pollack et al. 1996).

About 20% of Sun-like stars host super-Earths with radii of 1–4 $R_\oplus$ at distances of 0.05–0.3 au (Howard et al. 2010; Batalha et al. 2013; Petigura et al. 2013). Radial velocity measurements (Weiss & Marcy 2014) and transit timing variations (Wu & Lithwick 2013) manifest that the masses of these super-Earths are in the range of 2–20 $M_\oplus$. The abundance of super-Earths presents a puzzle for the core instability theory. This theory indicates that when a protoplanet reaches super-Earth size, two physical processes make the survival of super-Earths difficult, leading to a planetary "desert" in this size range (Ida & Lin 2004). Super-Earths excite density waves in protoplanetary disks (PPDs) and give rise to rapid type I migration. This type of migration causes the planet to be engulfed by its host star if the disk inner edge touches the stellar surface. Recent studies have sought various remedies for type I migration (Yu et al. 2011; Fung & Chiang 2017). PPDs are expected to have an inner edge at the stellar magnetosphere (e.g., Long et al. 2005). For planets undergoing disk-driven migration, they are expected to pile up near this edge. They stay either at the edge because the gas runs out, inside the edge down to 2:1 resonance because that is where the tidal torque tapers off, or outside the edge because the standing waves generated by wave reflection off the inner edge stall planet migration (Tsang 2011). In this paper, we focus on another threat for super-Earths. Super-Earths have low mean density, which suggests that they must be surrounded by gas envelopes (Rogers & Seager 2010). Since these observed super-Earths are in the range of critical mass, they trigger efficient gas runaway and accumulate massive gas envelopes. They become gas giants. As a result, super-Earths are supposed to be rare. However, *Kepler*'s discovery wrecks these predictions. Lee et al. (2014) proposed a metallicity gradient inside the PPDs or the late assembly of cores to resolve the puzzle of super-Earth formation. Lee & Chiang (2016) stressed that the late core assembly in transitional PPDs is more consistent with observations. In gas-poor environments, gas dynamical friction has weakened to allow proto-cores to stir one another and merge. In addition, this formation scenario ensures that

super-Earth cores accrete mass with a few percent envelope mass fraction (EMF).

Guillot & Showman (2002) argued that the dissipation of the kinetic energy of the atmospheric wind, driven by intense irradiation, could bury heat inside the planet. Many studies extend this idea to explain the radius anomaly of hot Jupiters (Youdin & Mitchell 2010; Ginzburg & Sari 2015; Komacek & Youdin 2017). These investigations focus on the late evolution after the disk dispersal. Unfortunately, this is invalid for the early evolution of super-Earths because they are still embedded within disks. The irradiation may not penetrate the disk and is not able to bury heat in the exoplanets.

However, we note that tidal interactions between the host star and planet can periodically perturb the planet and generate mechanical forcing of the fluid motions (Zahn 1977; Goldreich & Nicholson 1989). Heating by tidal dissipation in primordial super-Earth envelopes can inhibit gas cooling (Ginzburg & Sari 2017). This mechanism requires the orbital eccentricity of super-Earths to be continuously pumped. But super-Earths may not be massive enough to clear a clean gap to excite orbital eccentricity (Goldreich & Sari 2003). Another important aspect about tidal interaction is that tidally forced turbulent mixing induces heat transport inside the planets. Recent laboratory experiments show that turbulence could penetrate deep inside the planet interior (Cabanes et al. 2017). By combining laboratory measurements and high-resolution simulations, Grannan et al. (2017) confirmed the generation of bulk filling turbulence inside the planets driven by tidal forcing. Turbulent mixing plays an essential role in heat transport in strongly stratified environments (Garaud & Kulenthirarajah 2016). This motivates us to study the effects of turbulent diffusion on the planet's thermal evolution. Prior studies have noticed that the turbulent mixing induced by mechanical forcing leads to heat transport inside hot Jupiters (Youdin & Mitchell 2010). These tides produce appreciable thermal feedback and may lead to interior radiative zones, enhancing g-mode dissipations with a wide spectrum of resonances (Jermyn et al. 2017). We find that the thermal feedback associated with the externally forced turbulent stirring may greatly alter the accretion history of super-Earths.

It is well known that the timescale of gas accretion is dictated by the KH timescale. In other words, accretion is determined by the planet's ability to cool (Lee & Chiang 2015). In this paper, we note that the tidally forced turbulent diffusion influences the heat transport inside the planet's envelope. Thermal feedback is induced by turbulent diffusion. The heat transport associated with tidally forced turbulent diffusion reduces the cooling luminosity and enhances the KH timescale. We find that turbulent diffusion may have significant effects on the planet's accretion history.[1] Based on our calculations, we propose that tidally forced turbulent diffusion effectively helps super-Earths evade growing into gas giants.

This paper is structured as follows. In Section 2, we provide a brief description of the accreting planet envelope with tidally forced turbulent diffusion. In Section 3, we compare the planet interior thermal profile with and without turbulent diffusion and discuss the thermal feedback induced by turbulent diffusion, especially the shift of radiative-convective boundaries (RCBs). In Section 4, we depict the cooling luminosity variations and onset of gas runaway. The quasi-static KH evolution and critical turbulent diffusivity are discussed in Section 5. In Section 6, we discuss the mass-loss mechanisms for super-Earths and the limitation of super-Earth formation by turbulent diffusion. A summary and conclusions are given in Section 7.

[1] In our calculation, the turbulent diffusion coefficient $\mu_{\rm turb} \sim 10^7$–10^9 cm^2 s^{-1}, comparable to typical $\mu_{\rm turb} \sim 10^6$–10^{10} cm^2 s^{-1} in solar system planets (de Pater & Lissauer 2001).

2. Accreting Envelope with Tidally Forced Turbulence

Super-Earths are susceptible to runaway accretion (Pollack et al. 1996). The ability to accrete is determined by the planet's power to cool (Lee & Chiang 2015). How super-Earths avoid rapid gas runaway depends critically on the cooling history of the planet, which is closely related to the thermal structure of the envelope. In the convectively stable region, the turbulent diffusion induces heat transport within the planet. In this section, we concentrate on the thermal feedback caused by tidally induced turbulent diffusion.

2.1. Thermal Structure of the Gaseous Envelope

Since the planet's ability to cool depends on the thermal structure of the envelope, we first study the gaseous envelope structure of planets, i.e., the distribution of pressure, temperature, and mass around a protoplanetary core with mass $M_{\rm c}$ embedded within the protoplanetary nebula. The planet envelope (or "atmosphere") structure is governed by the following equations of mass conservation, hydrostatic equilibrium, thermal gradient, and energy conservation (Kippenhahn et al. 2012):

$$\frac{dM_r}{dr} = 4\pi\rho r^2, \tag{1}$$

$$\frac{dP}{dr} = -\frac{GM_r}{r^2}\rho, \tag{2}$$

$$\frac{dT}{dr} = \nabla\frac{T}{P}\frac{dP}{dr}, \tag{3}$$

$$\frac{dL}{dr} = \frac{dM_r}{dr}\left(\epsilon - T\frac{\partial s}{\partial t}\right), \tag{4}$$

where G is the gravitational constant, P is the pressure, ρ is the density, T is the temperature, L is the luminosity, and M_r is the mass, including the core mass and the atmosphere mass, enclosed inside the radius r, $M_r = M_{\rm atm} + M_{\rm c}$. The symbol ∇ denotes the temperature gradient inside the envelope. The energy generation ϵ is set to zero, since there is no nuclear reaction inside the planet. The above equations implicitly indicate that the envelope quickly adjusts and the dynamical timescale is shorter than the accretion timescale (Rafikov 2006). Note that the right-hand term, $-T\frac{\partial s}{\partial t}$, in the energy equation dictates the cooling process. Replacing the local energy equation with a global energy equation greatly reduces the numerical tasks, and we need only deal with ordinary differential equations (ODEs), rather than partial differential equations (PDEs; Lee et al. 2014; Piso & Youdin 2014). Details will be discussed in Section 3.

The energy transport in the convective region is very efficient, and the temperature gradient is[2]

$$\nabla = \nabla_{\rm ad} = \left(\frac{d\ln T}{d\ln P}\right)_{\rm ad}. \quad (5)$$

The convective and radiative layers of the envelope are specified by the Schwarzschild criterion: the atmosphere is stable against convection when $\nabla < \nabla_{\rm ad}$ and convectively unstable when $\nabla \geqslant \nabla_{\rm ad}$. Since the convective energy transport is efficient, $\nabla = \nabla_{\rm ad}$ in the convective region. The actual temperature gradient can be expressed as

$$\nabla = \min(\nabla_{\rm ad}, \nabla_{\rm rad}). \quad (6)$$

In this paper, we adopt a polytropic index $\gamma = 7/5$ for an ideal diatomic gas and the adiabatic gradient $\nabla_{\rm ad} = (\gamma - 1)/\gamma$. Note that the realistic equation of state (EOS) would change the value of $\nabla_{\rm ad}$, and its effects will be left for future studies.

The radiative temperature gradient

$$\nabla_{\rm rad} = \frac{3\kappa LP}{64\pi\sigma GM_r T^4}, \quad (7)$$

where κ is the opacity. In the upper part of the atmosphere, the exact value of κ is highly uncertain, because the amount of dust and the dust size distribution are not well constrained in PPDs. Lee et al. (2014) studied both dusty and dust-free atmospheres and found that the RCBs are determined by H_2 dissociation at an almost fixed temperature of ~2500 K for a dusty atmosphere. They also found that for a dust-free atmosphere, the radiative region keeps an almost isothermal temperature fixed by the envelope outer surface. Technically, the opacity laws can be written as a power law as a function of pressure and temperature whether or not the total opacity is dominated by dust grains. For these reasons, we adopt a power-law opacity (Rafikov 2006; Piso & Youdin 2014; Ginzburg et al. 2016) by assuming that

$$\kappa = \kappa_0 (P/P_0)^{\alpha} (T/T_0)^{\beta}. \quad (8)$$

Here we choose $\kappa_0 = 0.001\ {\rm cm^2\ g^{-1}}$, which allows our fiducial model without turbulent diffusion to possess properties of more sophisticated super-Earth models (Lee et al. 2014). What is important is the opacity near the RCB. In that sense, it is important to keep in mind that the power-law indices α and β can change significantly within the envelope (and with distance from the star). We have tried different choices of α and β. We find that, as long as the parameters α and β satisfy $\nabla_0 \equiv \frac{1+\alpha}{4-\beta} > \nabla_{\rm ad}$, our results are robust and insensitive to the choices we made.[3]

[2] This assumption is mainly made for simplicity of the models; they are not necessarily correct (Stevenson 1985; Leconte & Chabrier 2012). We are working on including the mixing-length theory (e.g., Kippenhahn et al. 2012) to better quantify the issue of super-adiabaticity.

[3] In a later part of this paper, we present the results with $\alpha = 1$, $\beta = 1$, which ensures the existence of the inner convective region and outer radiative region inside the planet gas envelope. For details, please refer to discussions in Rafikov (2006) and Youdin & Mitchell (2010).

Conventionally, it is believed that solid cores accrete planetesimals and gas simultaneously (Pollack et al. 1996; Bodenheimer et al. 2000). However, estimation shows that the termination epoch of the accretion of solids is well before that of the accretion of gas. The dust coagulation timescale can be as short as $t_{\rm coagulate} \sim 10^4$ yr, especially when the planet is close to the central host (Lee et al. 2014). This timescale is much shorter than the typical disk dispersal timescale (~0.5–10 Myr). In addition, calculations by Lee & Chiang (2015) showed that planetesimal accretion does not generically prevent runaway. As a result, it is physically valid to set the planetesimal accretion rate to zero ($L_{\rm acc} = 0$) when we study accreting super-Earths within the disk. In this case, the core is free to cool and contract, and it is extremely susceptible to gas runaway.

Note that the above differential equations are essentially identical to the usual planet interior structure equations. The distinction is the thermal feedback generated by tidally forced turbulent mixing inside the stably stratified region. More specifically, $\nabla_{\rm rad}$ is affected by turbulent diffusion, which will be further discussed in the next section.

2.2. Thermal Feedback by Tidally Forced Turbulent Mixing

How do super-Earths evade becoming gas giants? In this paper, we propose a robust mechanism to avoid runaway accretion. Due to tidal forcing, the planet's gas envelope is stirred, and turbulent motion may be initiated. Detailed analyses of these processes are rather complex and beyond the scope of this paper (e.g., Garaud & Kulenthirarajah 2016; Grannan et al. 2017). In this paper, we try to constrain the turbulent diffusion that is necessary to influentially affect the planet accretion timescale. We find that even weak turbulence affects the planet accretion history significantly.

Since the sound-crossing time is much shorter than the time for heat to diffuse across the fluid blob, the blob conserves entropy (i.e., adiabatically) and keeps pressure equilibrium with the ambient environments when it displaces over a radial distance ℓ. The temperature difference between the blob and its surroundings is

$$\delta T = \left(\frac{dT}{dr}\bigg|_{\rm ad} - \frac{dT}{dr}\right)\ell = -\frac{\ell T}{c_p}\frac{ds}{dr}. \quad (9)$$

The heat excess associated with these fluid blobs can be written as $\delta q = \rho c_p \delta T$, and the corresponding turbulent heat flux is $F_{\rm turb} = v\delta q$, where v is the characteristic speed of turbulent eddies. The entropy gradient can be put down as

$$\frac{ds}{dr} = \frac{g}{T\nabla_{\rm ad}}(\nabla_{\rm ad} - \nabla), \quad (10)$$

where g is the gravitational acceleration. This equation indicates that in the stably stratified region ($\nabla < \nabla_{\rm ad}$), the entropy gradient is positive ($ds/dr > 0$). The heat flux by turbulent mixing is then

$$F_{\rm turb} = v\delta q = \rho c_p v \delta T = -\rho g v\, \ell\left(1 - \frac{\nabla}{\nabla_{\rm ad}}\right). \quad (11)$$

The flux is negative for stable stratification. For a thermal engine without external forcing, heat always flows from hot to

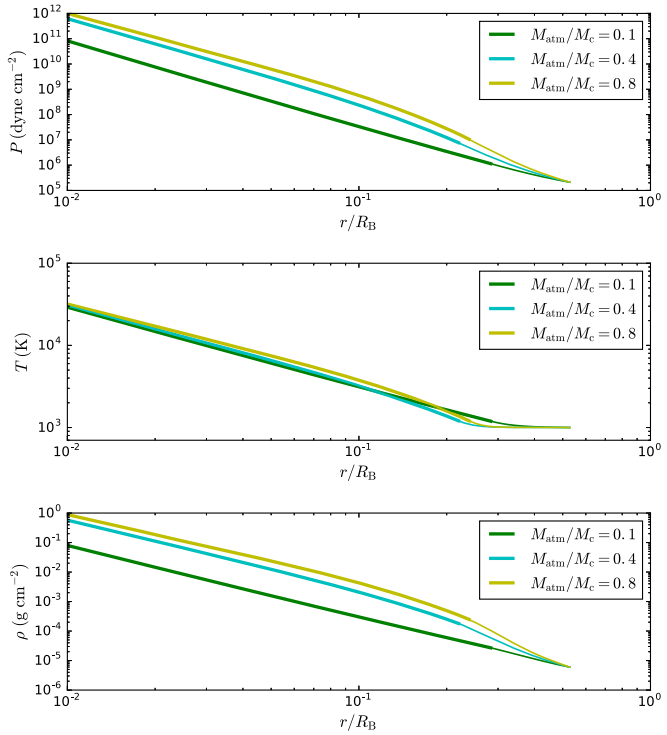

Figure 1. Thermal profiles around a planet core with mass $M_{\rm c}=5\ M_{\oplus}$ at 0.1 au. Turbulence is not included, $\nu_{\rm turb}=0$. The pressure, temperature, and density are shown in the upper, middle, and lower panels, respectively. In each panel, the green, cyan, and yellow lines stand for $M_{\rm atm}/M_{\rm c}=0.1$, 0.4, and 0.8, respectively. With the increase of envelope mass, the pressure at RCBs always increases. However, the position of the RCBs inside the planet first decreases and then increases. This nonmonotonic behavior is due to the effects of self-gravity (Piso & Youdin 2014). Note in particular that no pseudo-adiabatic region appears in the envelope (cf. Figure 2).

cold regions. However, with external mechanical forcing by tides, heat flow from cold to hot regions becomes feasible (Youdin & Mitchell 2010). Note that the turbulent diffusion coefficient $\mu_{\rm turb}\equiv v\ell$[4], and the corresponding luminosity is

$$L_{\rm turb}=4\pi r^2\left[-\rho g\mu_{\rm turb}\left(1-\frac{\nabla}{\nabla_{\rm ad}}\right)\right]. \tag{12}$$

The total luminosity is carried by two components, the radiative and the turbulent:

$$L=L_{\rm rad}+L_{\rm turb}. \tag{13}$$

We note that the temperature gradient in the radiative region can be arranged in a compact form as (see Appendix for details)

$$\nabla_{\rm rad}=\frac{1+\eta}{1/\nabla^{(0)}_{\rm rad}+\eta/\nabla_{\rm ad}}. \tag{14}$$

In the above equation,

$$\nabla^{(0)}_{\rm rad}\equiv\frac{3\kappa PL}{64\pi\sigma GM_r T^4}, \tag{15}$$

and

$$\eta\equiv\frac{4\pi\mu_{\rm turb}GM_r\rho}{L}=4\pi\left(\frac{M_{\rm c}}{M_{\oplus}}\right)\nu_{\rm turb}\left(\frac{M_r}{M_{\rm c}}\right)\left(\frac{\rho}{\rho_{\rm disk}}\right), \tag{16}$$

[4] Note that $\mu_{\rm turb}=K_{zz}$, a symbol widely used in the community of planetary atmospheres.

where the superscript (0) indicates the radiative temperature gradient without turbulence[5] and $M_{\rm c}$ is the mass of the solid core. It can be readily shown that the following inequality holds in the radiative region $\nabla^{(0)}_{\rm rad}<\nabla<\nabla_{\rm ad}$ (see Figure 3 for the pseudo-adiabatic region). Here we stress that it is the turbulent diffusion driven by external tidal forcing that makes ∇ steeper than $\nabla^{(0)}_{\rm rad}$. This inequality has significant implications for the thermal feedback induced by tidally forced turbulent diffusion. An interesting issue is that radiative zones are enlarged and the cooling luminosity is greatly reduced.

Here we define two dimensionless parameters:

$$\nu_{\rm turb}\equiv\frac{\mu_{\rm turb}}{L/(GM_{\oplus}\rho_{\rm disk})},\ \zeta\equiv\frac{\mu_{\rm turb}}{H_p c_s}. \tag{17}$$

The two parameters represent the strength of turbulence. In the definition of ζ, $H_p\equiv -dr/d\ln P$ and c_s are the pressure scale height and sound speed, respectively. It is obvious that, if the turbulence in the radiative region is negligible, i.e., $\eta=0$, the temperature gradient recovers its usual definition, $\nabla_{\rm rad}\rightarrow\nabla^{(0)}_{\rm rad}$. In Section 5.1, we give a physical estimation of the parameter ζ based on our calculations. We see that a small value of $\zeta\sim 10^{-6}$–10^{-5} already has appreciable effects on the formation of super-Earths. This mechanism is robust in the sense that even weak turbulence is adequate for it to operate. We should keep in mind that one limitation is that the turbulence strength is parameterized, not physically specified. This is an important issue that still remains to be addressed; i.e., forcing turbulence induced by tides should be investigated in further detail (Barker 2016; Grannan et al. 2017).

2.3. Boundary Conditions

The density and temperature at the outer boundary of the atmosphere are given by the nebular density and temperature. We adopt the minimum-mass extrasolar nebula (MMEN) model of Chiang & Laughlin (2013). According to MMEN, the disk structure reads

$$\rho_{\rm disk}=6\times 10^{-6}\left(\frac{a}{0.1\ {\rm au}}\right)^{-2.9}{\rm g\ cm^{-3}}, \tag{18}$$

$$T_{\rm disk}=1000\left(\frac{a}{0.1\ {\rm au}}\right)^{-3/7}{\rm K}. \tag{19}$$

The inner boundary lies at the surface of the inner core. The core density is assumed to be $\rho_{\rm core}=7\ {\rm g\ cm^{-3}}$, the core mass is $5\ M_{\oplus}$, and the core radius is $R_{\rm core}=1.6\ R_{\oplus}$. The outer boundary condition is chosen at the smaller of the Bondi radius and Hill radius, which are

$$R_H\approx 40\ R_{\oplus}\left[\frac{(1+{\rm EMF})M_{\rm core}}{5M_{\oplus}}\right]^{1/3}\left(\frac{a}{0.1\ {\rm au}}\right), \tag{20}$$

$$R_B\approx 90\ R_{\oplus}\left[\frac{(1+{\rm EMF})M_{\rm core}}{5M_{\oplus}}\right]\left(\frac{1000\ {\rm K}}{T}\right), \tag{21}$$

respectively.

[5] This equation is actually the same as Equation (7) in this paper.

3. Thermal Properties of Gas Envelopes

Since the thermal cooling timescale is intimately related to the planet's interior structure, we first describe the interior structure of the gaseous envelope. To avoid the complication induced by sandwiched convection-radiation structure inside the planet interior (Ginzburg & Sari 2015; Jermyn et al. 2017), we simply consider a two-layer model, i.e., a convective interior and a radiative exterior (Piso & Youdin 2014).

We adopt the assumption that the luminosity, L, is spatially constant, which is valid in the radiative region if the thermal relaxation timescale is shorter than the thermal times in the rest of the atmosphere. The validation of such an assumption is corroborated by Lee et al. (2014) and Piso & Youdin (2014). To get the thermal profiles within the envelope, a luminosity L is required to obtain $\nabla_{\rm rad}$ before we numerically integrate the structure equations. The spatially constant L is treated as an eigenvalue of the ODEs. To get the eigenvalue numerically, we first give a guess value of L and reiterate the integration until the mass at the core, $m(R_{\rm c})$, matches the actual mass, $M_{\rm c}$. Note that, once the luminosity is found, the location of the RCB can be specified accordingly.

3.1. Envelopes without Heat Transport by Turbulent Mixing

For the convenience of comparison, we first consider a fiducial model, i.e., an envelope without turbulence ($\nu_{\rm turb}=0$). In Figure 1, we show the radial profiles of the pressure, temperature, and density of the envelope for a $5\,M_{\oplus}$ core with increasing envelope mass during atmospheric growth. The green, cyan, and yellow lines denote an EMF = 0.1, 0.4, and 0.8, respectively. The thicker and thinner parts stand for the convective and radiative regions, respectively. The boundaries of the thicker and thinner parts are the RCBs. The convective region is adiabatic. The radiative region connects the lower entropy interior to the higher entropy exterior. In Figure 1, we note that the pressure in the convection zone increases with envelope mass, but the temperature only varies slightly. Since the entropy is $\propto \ln(T^{1/\nabla_{\rm ad}}/P)$, it is clear that, with increasing envelope mass, the steady-state envelopes evolve in order of decreasing entropy (Marleau & Cumming 2014). This is consistent with the cooling process that the envelope experiences, which allows the atmosphere to accrete more gas.

Lee et al. (2014) found that, for a dusty atmosphere, the locations of the RCBs lie at a roughly fixed temperature where H_2 dissociates (~2500 K). In Figure 1, the RCB lies at the bottom of the outermost radiative region, and the temperatures at the RCBs are no longer 2500 K. This is because we adopt a grain-free atmosphere due to efficient grain coagulation (Ormel 2014). According to the middle panel of Figure 1, we find that a grain-free atmosphere behaves differently from a grain-rich atmosphere. The outer radiative region is nearly isothermal, which implies that $T_{\rm RCB}\sim T_{\rm out}$. Such features have also been identified in Inamdar & Schlichting (2015) and Lee & Chiang (2015, 2016), which can be readily understood in terms of the following relation (Rafikov 2006; Piso & Youdin 2014):

$$\frac{T_{\rm RCB}}{T_{\rm out}}\sim\left(1-\frac{\nabla_{\rm ad}}{\nabla_0}\right)^{-1/(4-\beta)}\sim 1. \tag{22}$$

The term on the right-hand side of this equation is around the order of unity. This explains the temperature at the RCB, $T_{\rm RCB}\sim T_{\rm out}$. We stress that the above relation is only valid for an atmosphere without turbulence. When heat transport by turbulent mixing is taken into account, the RCB is pushed inward, and the temperature at the RCB ($T_{\rm RCB}$) becomes higher.

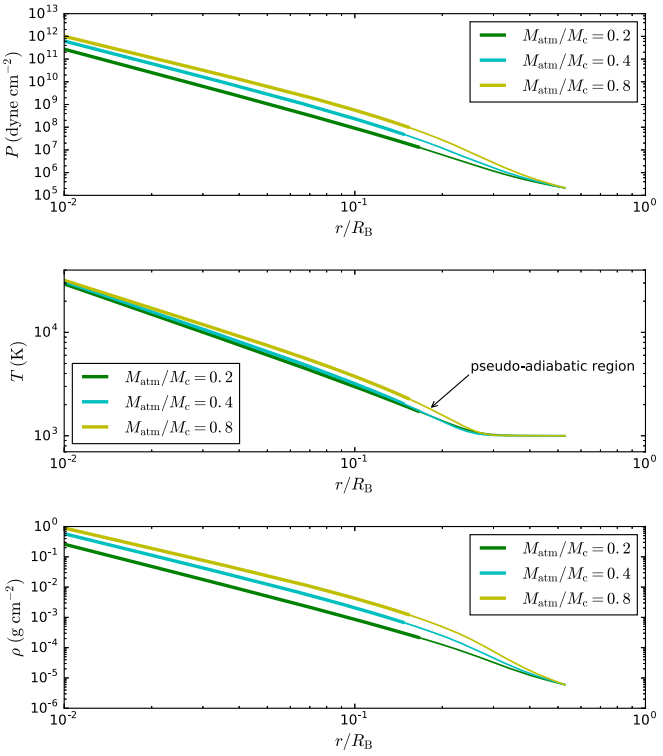

Figure 2. Same as Figure 1 but for a turbulent envelope with $\nu_{\rm turb}=0.016$. The pseudo-adiabatic region is most clearly visible when comparing the middle panels of Figures 1 and 2. Due to the presence of a pseudo-adiabatic region, the RCBs are pushed inward. The temperature at the RCBs becomes higher when heat transport by tidally forced turbulent mixing is taken into account.

At the early stage of accretion, the envelope mass is small, and the envelope can be well treated as non–self-gravitating. In this case, simple analytic results can be derived (Rafikov 2006; Piso & Youdin 2014). Though the envelope we consider in this paper is self-gravitating, these analytical results are still very instructive to understand atmospheric evolution and interpret our numerical results. How the position of the RCBs varies with envelope mass can be understood with the following relations (Piso & Youdin 2014):

$$\frac{M_{\rm atm}}{M_{\rm c}}=\frac{P_{\rm RCB}}{\xi P_{\rm M}},\quad \frac{P_{\rm RCB}}{P_{\rm disk}}\sim e^{R_{\rm B}/R_{\rm RCB}}, \tag{23}$$

where ξ is a variable on the order of unity and $P_{\rm M}$ is the characteristic pressure that is related to the core mass (Piso & Youdin 2014). In the early stage of planet accretion, with the increase of envelope mass, the pressure at the RCB increases as well. Accordingly, the cooling luminosity is reduced. When the self-gravity becomes important, the above relations no longer hold. The stronger luminosity is necessary to support the more massive envelope. With the increase of luminosity, the RCB is shifted outward, as shown in Figure 1 (Ginzburg & Sari 2015).

3.2. Envelopes with Heat Transport by Turbulent Mixing

In this section, we explore how turbulence ($\nu_{\rm turb}\neq 0$) changes the structure of the planet envelope. The most

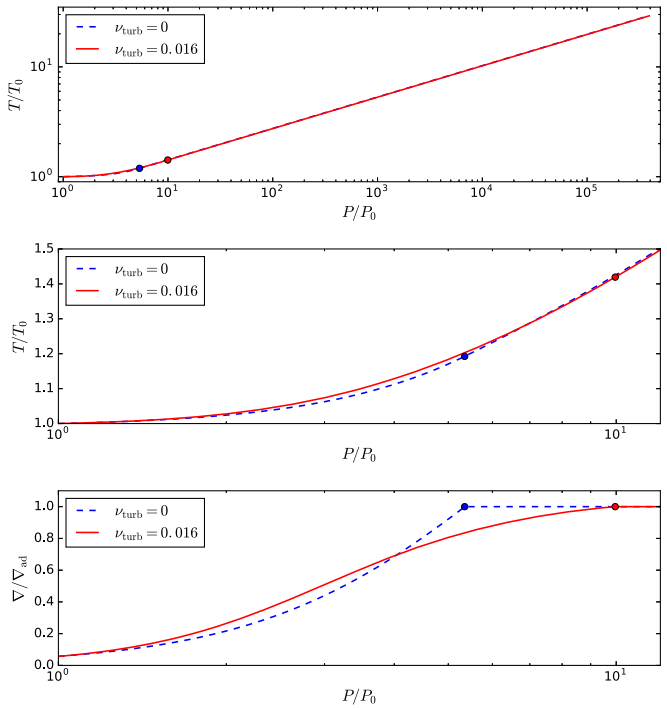

Figure 3. Thermal profiles of the planet envelope. The EMF $M_{\rm atm}/M_{\rm c}=0.1$. Upper panel: the blue dashed curve represents the envelope without turbulence. The red solid curve denotes the envelope with turbulence, $\nu_{\rm turb}=0.016$. The RCBs are denoted as blue and red dots. The two temperature profiles are very similar and difficult to distinguish. Middle panel: to identify their differences, we show the two profiles near the radiative-convective transition region. The red curve shows a more gradual transition from the radiative to adiabatic region. The region between the blue and red dots is the pseudo-adiabatic region. Bottom panel: ratio of temperature gradient to adiabatic gradient. The region with $\nabla/\nabla_{\rm ad}=1$ is the convection zone. The region with $\nabla/\nabla_{\rm ad}<1$ is the radiative zone. In the pseudo-adiabatic region, ∇ is very close to $\nabla_{\rm ad}$ but still smaller than $\nabla_{\rm ad}$. The RCBs shift inward when heat transport by turbulent mixing is taken into account. The RCBs penetrate deeper with stronger turbulent mixing.

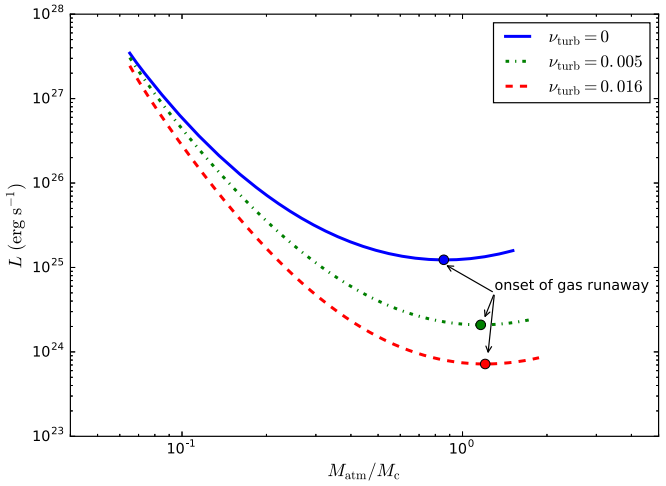

Figure 4. The luminosity L varies nonmonotonically with envelope mass. The results for $\nu_{\rm turb}=0$, 0.005, and 0.016 are shown with blue solid, green dot-dashed, and red dashed lines, respectively. The luminosity minimum is reached at $M_{\rm atm}/M_{\rm c}=0.86$, 1.16, and 1.20, respectively. When the envelope mass is small, its increase causes the luminosity to decrease. When the envelope mass is sufficiently large, the self-gravity of the gas envelope becomes important, and bigger luminosity L is necessary to support stronger gravity. We choose the luminosity minimum as the epoch when the runaway accretion sets in. We note that two important aspects of thermal evolution during planet accretion are affected. With the enhanced turbulence, the cooling luminosity is reduced globally. When the turbulence becomes stronger, the onset of gas runaway occurs at a higher EMF.

interesting feature is that turbulence pushes the RCBs inward and diminishes the cooling luminosity. In Figure 2, we show the planet thermal profiles for EMF, $M_{\rm atm}/M_{\rm c}=0.2$, 0.4, and 0.8. The core mass $M_{\rm c}=5\ M_{\oplus}$. In Figure 2, we find that the difference is that a pseudo-adiabatic region appears. Explicitly, we point out the location of the pseudo-adiabatic region in the middle panel of Figure 2. In such regions, the temperature gradient is very close to the adiabatic gradient but still smaller than the adiabatic gradient (see Figure 3).

From the middle panel of Figure 1, we see that, when heat transport by turbulent diffusion is not included, the RCB lies around the isothermal radiative region, $T_{\rm RCB}\sim T_{\rm out}$. When turbulent diffusion is included, the temperature gradient deviates from the isothermal approximation, which is most obvious by comparing the middle panels of Figures 1 and 2. We can identify from Figure 3 that the temperature gradient near the RCBs is approaching $\nabla_{\rm ad}$ and clearly deviates from the isothermal temperature gradient. Due to this temperature gradient deviation, a pseudo-adiabatic region appears. As a result, the temperature at the RCB becomes higher, and the RCBs penetrate deeper inside the envelope.

To better understand the effects of heat transport by turbulent mixing, we compare the profiles of the planet envelope with and without turbulence. The results are shown in Figure 3 as red solid and blue dashed lines, respectively. The upper panel shows the global variation of temperature with pressure within the envelope. In this panel, the difference between the cases with and without turbulence is hardly discernible. The middle panel shows the variation of temperature with pressure but focuses on the localized region around the radiative-convective transition region. It shows that turbulent mixing smooths the transition toward the adiabat. There appears to be a pseudo-adiabatic region above the actual adiabatic region. This pseudo-adiabatic region pushes the RCB inward to higher pressure. Turbulent mixing leads to a more gradual approach to the adiabat.

The turbulent diffusion in the stably stratified region provides heating instead of cooling, so it is natural to expect that with turbulent diffusion taken into account, the total cooling rate of the envelope will decrease and the KH contraction timescale will be prolonged (see Figure 4 for details).

4. Onset of Gas Runaway and Cooling Luminosity Variations

Since we are interested in the planet accretion history, it is necessary to investigate the luminosity with increasing envelope mass. In the deep atmosphere, heat is advected by convective eddies. Near the surface, this could be achieved by diffusion. The surface temperature gradients become shallower, and a radiative region shows up. The variations of luminosity with envelope mass are shown in Figure 4. With the accumulation of envelope mass, the luminosity reaches a minimum. Beyond this minimum, the luminosity L increases. As a result, the planet begins to cool at a very short timescale, and the envelope mass grows superlinearly after this epoch. Physically, it is natural to adopt the epoch when the minimum L is reached as the onset of gas runaway, $t_{\rm run}$.

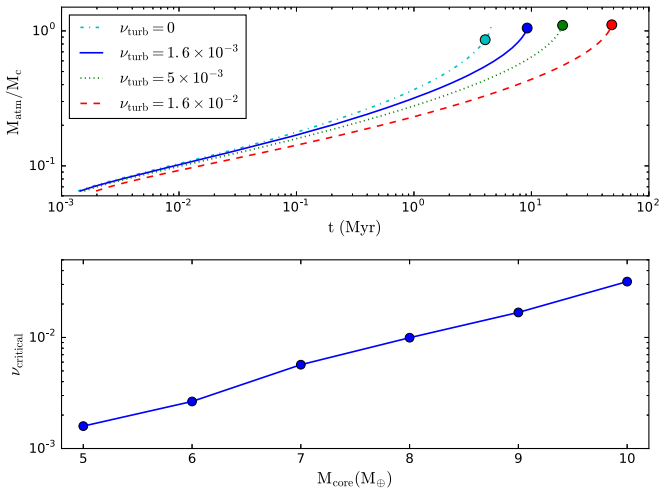

Figure 5. Upper panel: the accretion history for $\nu_{turb} = 0$, 0.0016, 0.005, and 0.016 is shown as cyan dot-dashed, blue solid, green dotted, and red dashed lines, respectively. The initial time for the accretion is estimated as $t_0 = |E|/L$. The slightly different starting time is due to the luminosity decrease by the inclusion of turbulence (see Figure 4). The initial EMF is around 6%, where the planet is nearly fully convective. Different colored dots in the upper panel denote the epoch, t_{run}, when the gas runaway takes place. The runaway time is $t_{run} = 4.04$, 10, 18.4, and 48.3 Myr, respectively. The solid blue curve shows the critical solution, where $t_{run} = t_{disk}$. The critical diffusivity for $M_{core} = 5$ $M_\oplus$ is $\nu_{critical} \sim 1.6 \times 10^{-3}$ if $t_{disk} = 10$ Myr. Lower panel: critical $\nu_{critical}$ for various core masses. For higher core masses, the critical $\nu_{critical}$ is higher. We note that weak turbulence with small diffusivity, $\mu_{turb} \sim 10^7$–10^8 cm^2 s^{-1}, can already enhance the runaway timescale and delay the gas runaway.

On the right-hand side of the luminosity minimum, the luminosity–mass relation is relatively easy to understand. At this late stage of mass growth, the self-gravity of the envelope appears to be prominent, and greater luminosity is necessary to support stronger gravity. However, on the left-hand side of the luminosity minimum, the mass of the envelope is small, and the planet is at the early stage of mass growth. At this early stage (the envelope's self-gravity can be ignored), the luminosity diminishes with a thicker radiative outer layer and more massive envelope. This reduction in cooling luminosity is intimately related to the shift of the RCBs. When the envelope self-gravity can be ignored, the luminosity at the RCB can be written as (Piso & Youdin 2014)

$$L_{RCB} = \frac{64\pi\sigma G M_{RCB} T_{RCB}^4 \nabla_{ad}}{3\kappa P_{RCB}} \approx \frac{L_{disk} P_{disk}}{P_{RCB}}, \quad (24)$$

where M_{RCB} and L_{disk} are

$$M_{RCB} = \frac{5\pi^2}{4} \rho_{RCB} R_B' \sqrt{R_{RCB}}, \quad L_{disk} \approx \frac{64\pi\sigma G M_{RCB} T_{disk}^4}{3\kappa_d P_{disk}} \nabla_{ad}. \quad (25)$$

The above equations can be written in terms of known properties if the envelope mass is centrally concentrated (see, e.g., Lee & Chiang 2015). This central concentration is physically expected since in deeper layers, where temperatures rise above ~2500 K, hydrogen molecules dissociate. As energy is spent on dissociating H_2 molecules rather than heating up the gas, the adiabatic index drops below 4/3 to approach 1. The upshot is that both the densities at the RCB and the radiative luminosity can be written in terms of core properties and the temperature at the RCB.

As the RCB deepens, it becomes even more optically thick, so it is harder to radiate energy away; as a result, the envelope cools more slowly.

In Figure 4, we stress that two important aspects of thermal evolution during planet accretion would be affected by turbulent mixing. The first is that it influences the luminosity. In Figure 4, we know that when the turbulent diffusivity (ν_{turb}) is enhanced, the cooling luminosity is reduced globally. That is, for any particular value of envelope mass, the cooling luminosity for an envelope with turbulence is always below that without turbulence. When the turbulence is stronger, the luminosity becomes even smaller. The second is that it changes the EMF at which gas runaway occurs. In Figure 4, our calculations show that, when the turbulence becomes stronger, the onset of gas runaway takes place at a higher EMF.

5. Quasi-static KH Evolution and Critical Turbulent Diffusivity

Since we ignore the accretion luminosity from the planetesimals, the gravitational KH contraction is the only source for the cooling. The gas accretion is regulated by the KH timescale. Our time evolution model can follow the envelope mass growth up to the very early epoch of runaway growth around the crossover mass. Fortunately, Pollack et al. (1996) found that the timescale spent in the runaway accretion stage is orders of magnitude smaller than the KH timescale. The mass growth timescale is actually dominated by the KH stage. For this reason, our model can get a rather accurate estimation of the mass growth timescale of an accreting planet. In this section, we explore how turbulent mixing affects the KH contraction timescale. For strong turbulent diffusion, the heat transport may even inflate the planet (Youdin & Mitchell 2010). We are not interested in planet inflation induced by strong turbulence in this paper. We find that even weak turbulence can already play an essential role in delaying the KH contraction.

5.1. Time Evolution: Temporally Connecting Snapshots

In the previous section, we obtained snapshots of envelope structure for different envelope masses. To estimate the accretion timescale, we need to connect them temporally in order of increasing mass. The gas accretion history can be followed by the cooling process (Piso & Youdin 2014). Detailed estimation shows that the luminosity generated in the radiative region can be safely ignored (Lee et al. 2014). It is physically valid to assume that the luminosity of the envelope is generated in the convective zone and the luminosity can be treated as constant in the outer radiative zone (Piso & Youdin 2014). This greatly simplifies our evolutionary calculations. Under such circumstances, we only need to solve a set of ordinary differential equations and connect the solutions in time. Lee & Chiang (2015) showed that it is physically valid to omit planetesimal heating during the gas accretion of super-Earths. When there is no planetesimal accretion to power the gas envelope, the time interval between two adjacent hydrostatic snapshots is the time it takes to cool between them. In addition to internal energy variations, gas accretion and envelope contraction also bring about changes to the global energy budget. Specifically, the time interval between two

steady-state solutions can be written as (Piso & Youdin 2014)

$$\Delta t = \frac{-\Delta E + \langle e\rangle \Delta M - \langle P\rangle \Delta V_{\langle M\rangle}}{\langle L\rangle}. \quad (26)$$

Note that Δ designates the difference between the two adjacent states, and the brackets denote the average of them. The total energy E consists of the internal energy and the gravitational potential energy, which reads

$$E = \int_{M_c}^{M} u\, dM_r - \int_{M_c}^{M} \frac{GM_r}{r} dM_r, \quad (27)$$

where u is the specific internal energy, $u = c_v T$. The second term in Equation (26) stands for contribution from gas accretion. The specific energy of the accreting gas is $e = -GM_r/r + u$. The third term in Equation (26) accounts for PdV work done by the envelope contraction. All terms are calculated at the RCB. Note in particular that the volume differences between two adjacent snapshots are performed at fixed mass. We choose the fixed mass as the average of the masses at the RCB (Piso & Youdin 2014).

In the upper panel of Figure 5, we show the planet mass growth history for different turbulent diffusivity. In our fiducial model without turbulence, $t_{\rm run} \sim 4.04$ Myr. Beyond this epoch, the gas runaway occurs. The gas runaway is due to the fast increase of L beyond $t_{\rm run}$, which leads to a rapid cooling process on a shorter timescale. The most intriguing feature is that the runaway time is delayed and the accretion timescale is prolonged when heat transport by tidally forced turbulent mixing is taken into account. For instance, when $\nu_{\rm turb} = 0.0016$, 0.005, and 0.016, the runaway time $t_{\rm run} = 10$, 18.4, and 48.3 Myr, respectively. The stronger the turbulence, the longer the gas runaway timescale.

In our calculations, we find that a small value of $\nu_{\rm turb}$, on the order of 10^{-3}, can already appreciably affect the cooling timescale of super-Earths. Since $\nu_{\rm turb}$ is dimensionless, it is better to recover its physical value according to Equation (17). Typically, luminosities for super-Earths are $L \sim 10^{26}\,{\rm erg\,s^{-1}}$, $M_\oplus = 5.97 \times 10^{27}$g, and $\rho_0 = 6 \times 10^{-6}\,{\rm g\,cm^{-3}}$. Then, the term $L/(GM_\oplus\rho_0)$, defined in Equation (17), is approximately $\sim 4.2 \times 10^{10}\,{\rm cm^2\,s^{-1}}$. For the dimensionless diffusivity $\nu_{\rm turb} = 0.0016$, the physical diffusivity is approximately $\mu_{\rm turb} \sim 4.2 \times 10^7\,{\rm cm^2\,s^{-1}}$. For even larger $\nu_{\rm turb}$, the KH contraction timescale can be enhanced by orders of magnitude. According to Figure 5, it is evident that the turbulent diffusivity on the order of $\sim 10^7$–$10^8\,{\rm cm^2\,s^{-1}}$ can already enhance the runaway timescale by an order of magnitude. The pressure scale height inside the planet is $H_p \sim 10^9$ cm, and the sound speed is $c_s \sim 10^5\,{\rm cm\,s^{-1}}$. We can get a physical sense of how large the turbulent diffusivity is by estimating the dimensionless parameter ζ in Equation (17). In our calculation, ζ is pretty small, on the order of $10^{-7} \sim 10^{-6}$. This means that the turbulent diffusion necessary to prolong the cooling timescale needs to not be very strong.

5.2. Critical Turbulence Diffusivity $\nu_{critical}$ and Super-Earth Formation

A gas giant is formed if the PPD is still full of gas when the planet enters the runaway accretion stage. However, if the runway time $t_{\rm run}$ is longer than the disk lifetime $t_{\rm disk}$, the disk gas is depleted, and the planet is unable to accrete sufficient gas

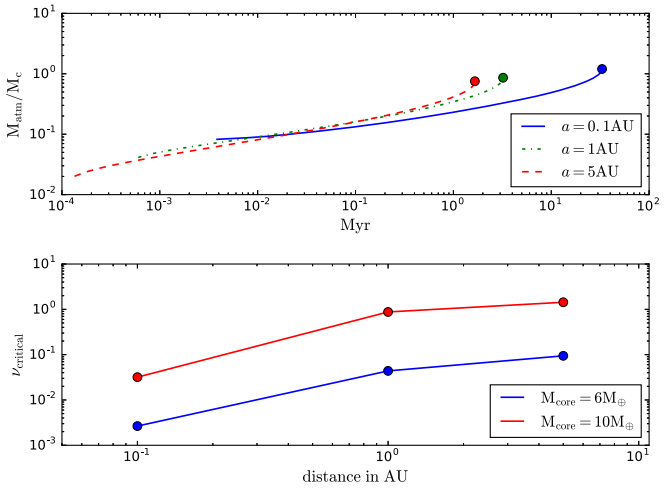

Figure 6. Upper panel: variations of envelope mass with time. The core mass is $M_c = 6\,M_\oplus$. The turbulent diffusivity is $\nu_{\rm turb} = 0.01$. The blue solid, green dot-dashed, and red dashed lines denote the mass growth history for planets at 0.1, 1, and 5 au, respectively. The critical mass ratio at the epoch of runaway decreases for more distant planets. The runaway times for the three different cases are 33.1, 3.2, and 1.7 Myr, respectively. It is expected that for more distant planets, larger turbulent diffusivity is required to prevent runaway gas accretion within $t_{\rm disk} \sim 10$ Myr. Lower panel: critical diffusivity, $\nu_{\rm critical}$, for different orbital locations, required to prevent gas runaway for a disk lifetime $t_{\rm disk} \sim 10$ Myr. Beyond $\nu_{\rm critical}$, the KH timescale is longer than the disk lifetime. The formation of super-Earths becomes possible.

to become a gas giant, then a super-Earth may be formed. Two timescales, $t_{\rm run}$ and $t_{\rm disk}$, determine the ultimate destiny of the planet, i.e., whether the planet becomes a super-Earth or a gas giant. If $t_{\rm run} < t_{\rm disk}$, gas runaway occurs within the lifetime of the disk. The planet gets inflated by the runaway gas accretion and become a gas giant. On the contrary, if $t_{\rm run} > t_{\rm disk}$, the disk disperses before the gas runaway takes place. Because there is not enough gas material for the planet to accrete, it is unable to become a gas giant. Usually, the disk life is about 5–10 Myr. To be specific, we take the disk lifetime as $t_{\rm disk} = 10$ Myr throughout this paper.

In the upper panel of Figure 5, the core mass is fixed at $M_{\rm core} = 5\,M_\oplus$. We find that there exists a critical diffusivity $\nu_{\rm critical} = 1.6 \times 10^{-3}$. When $\nu_{\rm turb} > \nu_{\rm critical}$, the KH contraction timescale becomes longer than the disk lifetime, and the core is not able to experience the gas runaway. In this case, the formation of gas giants can be avoided, and the formation of super-Earths becomes viable. In the lower panel of Figure 5, we show the variations of $\nu_{\rm critical}$ with $M_{\rm core}$. The critical diffusivity becomes larger when the core mass increases. Specifically, for a 10 $M_\oplus$ core, the critical dimensionless diffusivity is approximately $\nu_{\rm critical} = 3.2 \times 10^{-2}$. The actual diffusivity is about $\sim 10^9\,{\rm cm^2\,s^{-1}}$.

5.3. Variations of $\nu_{critical}$ with Planet Location in PPDs

Observationally, the *Kepler* statistics show that ~20% of Sun-like stars harbor super-Earths at distances of 0.05–0.3 au. By contrast, the occurrence rate for hot Jupiters inside ~0.1 au is only 1%. To explain these observational features, we consider how the turbulence affects the thermal evolution for planets at different locations in PPDs. The turbulent mixing considered in this paper is driven by the tides raised by the host star. We believe that the tidally induced turbulent mixing inside the planet becomes weaker when the planet is farther away from the host star.

Lee et al. (2014) found that, for a dusty disk, the runaway timescale is independent of the orbital location. However, since dust cannot persist in the envelope due to coagulation and sedimentation (Mordasini et al. 2014; Ormel 2014), the runaway timescale is no longer independent of the orbital location. In the upper panel of Figure 6, we show the accretion history for planets at three different locations. The core mass is $M_c = 6\ M_\oplus$. The blue solid, green dot-dashed, and red dashed curves designate the temporal variations of envelope mass for $a = 0.1$, 1, and 5 au, respectively. The turbulent diffusivity is $\nu_{\rm turb} = 0.013$. The gas runaway occurs at $t_{\rm run} = 33.1$, 3.2, and 1.7 Myr. It is clear that gas accretion onto cores is hastened for planets that are farther away from the central star. This behavior can be understood from the decrease in opacity at the RCB that makes the envelope more transparent, enhancing the rate of cooling (Inamdar & Schlichting 2015; Lee & Chiang 2015). The planets at $a = 1$ and 5 au become gas giants due to runaway accretion ($t_{\rm run} < t_{\rm disk}$). However, the planet in the inner region, $a = 0.1$ au, becomes a super-Earth ($t_{\rm run} > t_{\rm disk}$). The fact that atmospheres cool more rapidly at large distances as dust-free worlds has been used to explain the presence of extremely puffy, low-mass planets (Inamdar & Schlichting 2015; Lee & Chiang 2016).

We explore the critical diffusivity, $\nu_{\rm critical}$, for planets at different locations inside the MMEN. The results are shown in the lower panel of Figure 6. It shows that the critical diffusivity increases with the semimajor axis. When the planet is farther from the central star, $\nu_{\rm critical}$ becomes larger. This means that the more distant planet requires stronger turbulence to lengthen the KH timescale and avoid gas runaway. For tidally induced forcing, we believe that the turbulent diffusion $\nu_{\rm turb}$ is determined by the tides inside the planet raised by the host star. The tides become weaker if the planet is farther away from the host star. Our proposed mechanism can naturally explain the formation of a close-in super-Earth, while still ensuring the gas giant formation at a larger orbital distance. When the planet is near the host star, tidally forced turbulent mixing is stronger and $\nu_{\rm turb}$ is larger. According to Figure 6, the required threshold $\nu_{\rm critical}$ is smaller. As a result, the inequality $\nu_{\rm turb} > \nu_{\rm critical}$ can be more readily satisfied, and formation of a super-Earth becomes possible. On the contrary, when the planet is far from the host star, $\nu_{\rm turb}$ becomes smaller as the stirring by tides becomes weaker. The required threshold $\nu_{\rm critical}$ becomes larger. The threshold to avoid gas runaway is more difficult to satisfy. This indicates that, in the in situ planet formation scenario, it is more ready to form close-in super-Earths, and gas giants are more prone to appear in the outer region of PPDs. The above implication is consistent with the occurrence rate inferred from observations.

6. Mass-loss Mechanisms

Observation shows that super-Earths possess hydrogen and helium envelopes containing only several percent of the planet's mass. However, we can see in Figure 5 that the planets accrete very massive gas envelopes. The planet core with $\nu_{\rm turb} = 0$ reaches an EMF of $\sim$0.8 at the epoch of gas runaway. The envelope mass is considerably higher than the mass inferred from observations. These primordial super-Earths may experience significant mass loss during the post-formation evolution.

How super-Earths lose their mass still remains an open question. Here we briefly mention some possible ways to lose the envelope mass. The first possibility is that close-in planets are exposed to intense extreme UV and X-ray (XUV) irradiation from their host stars. Photoevaporation can significantly modify the structure of their atmospheres. Over the timescale of $\sim$100 Myr, X-rays from host stars can photoevaporate the super-Earth envelopes from an initial EMF of $\sim$1 to an EMF of $\sim$0.01–0.1, which may naturally explain the differences between the theoretical predictions and observational facts (e.g., Murray-Clay et al. 2009; Owen & Wu 2013, 2017; Gaudi et al. 2017).

Giant impact is the second possible mechanism to explain the mass loss, which is expected to be common because they are needed to provide long-term orbital stability of planetary systems (Cossou et al. 2014). Hydrodynamical simulations show that a single collision between similarly sized exoplanets can easily reduce the envelope–to–core mass ratio by a factor of two. Super-Earths' asymptotic mass can be achieved by one or two giant impacts. Under certain circumstances, almost 90% of the gas envelope can be lost during the impact process (Liu et al. 2015; Inamdar & Schlichting 2016).

Mass transfer between the close-in planet and host star via Roche lobe represents the third way to reduce the planet mass (Valsecchi et al. 2015; Jackson et al. 2017; Jia & Spruit 2017). Tidal dissipation can drive the orbits of these primordial super-Earths to decay toward the Roche limit. The mass transfer is quite rapid, potentially leading to complete removal of the gaseous envelope in a few Gyr and leaving behind a super-Earth. Many gaseous exoplanets in short-period orbits are on the verge or in the process of Roche-lobe overflow (RLO). The coupled processes of orbital evolution and RLO likely shape the observed distribution of close-in exoplanets and may even be responsible for producing some of the short-period rocky planets. But recent calculations by Dosopoulou et al. (2017) challenged this idea by claiming that, for highly eccentric or retrograde planets, self-accretion by the planet slows down the mass-loss rate via RLO.

Super-Earth EMFs are in the range of just 1%–10% and more typically are just $\sim$1% (see Rogers & Seager 2010; Lopez & Fortney 2014; Wolfgan & Lopez 2015). The mechanism discussed in this paper overpredicts the EMF of super-Earths, often beyond 80%. Photoevaporation, even around Sun-like stars, is only effective out to 10 days, and many super-Earths lie beyond this (see, e.g., Figure 8 of Owen & Wu 2013). Removal of >90% of the envelope by giant impact requires an impact velocity that exceeds the escape velocity (see, e.g., Figure 3 of Inamdar & Schlichting 2016). Finally, RLO only works within two stellar radii of where the Roche radius is. Lee & Chiang (2016) proposed that the late-time formation of cores ensures that super-Earth cores accrete a few percent EMF, in agreement with the observations. There is a clear difference in the expected final EMF between their work and ours.

Very recent works have revealed that planetary envelopes embedded within PPDs may not be in hydrostatic balance, which slows down envelope growth. It is possible that a steady-state gas flow enters through the poles and exits in the disk midplane (Lambrechts & Lega 2017). In the presence of a magnetic field and weakly ionizing winds, ohmic energy is dissipated more readily for lower-mass planets. Ohmic dissipation would make super-Earths more vulnerable to atmospheric evaporation (Pu & Valencia 2017). These findings may offer new explanations for the typical low-mass envelopes around the cores of super-Earths. In addition, we also note that

the turbulent diffusion mechanism may be still operating in the late core assembly scenario. In the late core assembly scenario without turbulent diffusion, the asymptotic EMF is about 3%–5% (Lee & Chiang 2016). When turbulent diffusion is taken into account, the EMF can be further reduced to 1%.

7. Summary and Conclusion

In this paper, we propose a new mechanism to avoid gas runaway for planet cores within the lifetime of disks. The mechanism proposed in this paper is not subject to the κ or μ catastrophe (Lee & Chiang 2015). Tidal heating (Ginzburg & Sari 2017) requires orbital eccentricity be continuously pumped up during super-Earth formation. Our mechanism does not depend on the orbital eccentricity of a super-Earth. Incorporating this model into a population synthesis model may better constrain our understanding of exoplanet formation (Ida & Lin 2004; Jin & Mordasini 2017).

We have explored the effects of heat transport induced by tidal stirring on the thermal structure of stably stratified, radiative layers of super-Earths, focusing on their influences on the KH timescale. When we take turbulent stirring into account, pseudo-adiabatic regions show up within the radiative zone. This may push the RCBs inward. The temperature and pressure at the RCBs becomes higher, and the cooling luminosity is reduced. As a result, the KH timescale is enhanced. We find that there exist a critical turbulent diffusivity $\nu_{\rm critical}$. When $\nu_{\rm turb} > \nu_{\rm critical}$, the runaway time is greater than the disk lifetime ($t_{\rm run} > t_{\rm disk}$). Under such circumstances, the onset of the planet gas runaway lags behind the disk gas depletion. Since the planet does not have enough gas to accumulate, it can no longer grow into a gas giant and becomes a super-Earth instead. In addition, we also investigate the variations of $\nu_{\rm critical}$ with the planet's semimajor axis in MMEN. Our calculations show that the condition for turbulence-induced formation of super-Earths is more readily satisfied in the inner disk region but is harder to satisfy in the outer disk region. The occurrence rate of super-Earths and gas giants is consistent our calculations.

The extent of the radiative region has important implications for the tidal dissipations inside the planet. The turbulence pushes the RCBs inward and produces enlarged radiative zones. Since the internal gravity waves can propagate inside the radiative zone, the variations of this resonant cavity significantly influence the dissipation of internal gravity waves. This greatly influences the propagation and dissipation of internal gravity waves inside the radiative zone (Jermyn et al. 2017). Another effect is that the transition between the convective and radiative zones is smoothed. The radiative zone is thickened, and this bears important implications for internal gravity wave excitation and propagation (Lecoanet & Quataert 2013). This has appreciable effects on the thermal tides inside the planet. These issues will be addressed in a further study.

A limitation of this work is that the turbulence strength is not specified from first principle. As a compromise, we parameterize the turbulence diffusion as a free parameter. We try to constrain the turbulence strength in terms of the planet thermal evolution. Interestingly, we find that turbulence in the radiative region has substantial effects on the planet's accretion history. How turbulence is initiated during planet formation and how strong the turbulent diffusion is involve very complicated physical processes, which are worth further investigation.

Realistic opacities and EOSs have influential effects on the planetary thermal structure and core-accretion process (e.g., Stevenson 1982; Ikoma et al. 2000; Rafikov 2006), especially for the timescale of the KH timescale (Lee et al. 2014; Piso & Youdin 2014). Our simple prescription of opacity needs to be improved. Guillot et al. (1994) showed that a convective layer lies between two adjacent radiative regions due to the opacity window near $\sim$2000 K. A relevant caveat is the existence of radiative zones sandwiched inside the convective interior. Such radiative windows are ignored in our two-layer models. It would be interesting to consider how a downward turbulent heat flux interacts with such a sandwiched region. In summary, how the super-Earth envelope cooling history responds to more realistic opacities and EOSs needs to be further investigated. Calculations with realistic EOSs and opacity are underway and will be reported elsewhere.

We have found that the epoch of runaway accretion can be effectively delayed by the turbulent diffusion within the stably stratified region. But we should be cautious that the EMF predicted by this mechanism is not fully consistent with observations. The EMF for a planet embedded within the gas-rich MMEN is greater than 80%, much higher than the typical super-Earth envelope. It is difficult for the turbulent diffusion alone to make the EMF be consistent with observations. Additional physical processes, such as giant impact, photo-evaporation, and RLO, may be operating to reduce the EMF during the formation of super-Earths. But these mass-loss processes either operate on distances shorter than most super-Earths or are applicable under certain circumstances. A promising mechanism for super-Earth formation is the late core assembly within the transitional PPDs. In this scenario, with the reduction of the PPD mass density, the EMF can be as low as 3%–5% (Lee & Chiang 2016). We note that turbulent diffusion may still be working in the late core assembly scenario. How turbulent diffusion affects the EMF within transitional PPDs is an interesting issue worth further investigation.

We thank the anonymous referee for the thoughtful comments that greatly improved this paper. Discussions about heat transport inside planet interiors with Yanqin Wu and Re'em Sari are highly appreciated. This work has been supported by the National Natural Science Foundation of China (grants 11373064, 11521303, and 11733010), Yunnan Natural Science Foundation (grant 2014HB048), and Yunnan Province (2017HC018).

Appendix
Temperature Gradient with Turbulence

When the turbulent flux is taken into account, the luminosity can be written as

$$L = 4\pi r^2\left(-\frac{16\sigma T^3}{3\kappa\rho}\frac{dT}{dr}\right) + 4\pi r^2\left[-\mu_{\rm turb}\rho g\left(1-\frac{\nabla}{\nabla_{\rm ad}}\right)\right]. \tag{28}$$

Note that in the above equation, $g = GM_r/r^2$ and $\nabla = \frac{d\ln T}{d\ln P}$. This equation can be expressed as

$$\frac{dT}{dr} = \frac{L + 4\pi r^2\mu_{\rm turb}\rho\frac{GM_r}{r^2}}{\frac{16\sigma T^3}{3\kappa\rho} + \mu_{\rm turb}\frac{P}{\nabla_{\rm ad}T}}\left(-\frac{1}{4\pi r^2}\right). \tag{29}$$

If we take the pressure P as the independent variable, the temperature gradient becomes

$$\nabla = \frac{P}{T}\frac{dT}{dP} = \frac{1 + \frac{4\pi\mu_{\rm turb}GM_r\rho}{L}}{\frac{64\pi GM_r\sigma T^4}{3\kappa PL} + \frac{4\pi\mu_{\rm turb}GM_r\rho}{L}\frac{1}{\nabla_{\rm ad}}} = \frac{1+\eta}{1/\nabla^{(0)}_{\rm rad} + \eta/\nabla_{\rm ad}}, \quad (30)$$

where $\eta = 4\pi\mu_{\rm turb}GM_r\rho/L$.

ORCID iDs

Cong Yu https://orcid.org/0000-0003-0454-7890

References

Arras, P., & Socrates, A. 2010, ApJ, 714, 1
Barker, A. J. 2016, MNRAS, 459, 939
Batalha, N. M., Rowe, J. F., Bryson, S. T., et al. 2013, ApJS, 204, 24
Bodenheimer, P., Hubickyj, O., & Lissauer, J. J. 2000, Icar, 143, 2
Bodenheimer, P., & Pollack, J. B. 1986, Icar, 67, 391
Cabanes, S., Aurnou, J., Favier, B., & Le Bars, M. 2017, NatPh, 13, 387
Chiang, E., & Laughlin, G. S. 2013, MNRAS, 431, 3444
Cossou, C., Raymond, S. N., Hersant, F., & Pierens, A. 2014, A&A, 569, 56
de Pater, I., & Lissauer, J. J. 2001, Planetary Sciences (Cambridge: Cambridge Univ. Press)
Dosopoulou, F., Naoz, S., & Kalogera, V. 2017, ApJ, 844, 12
Fung, J., & Chiang, E. 2017, ApJ, 839, 100
Garaud, P., & Kulenthirarajah, L. T. 2016, ApJ, 821, 49
Gaudi, B. S., Stassun, K. G., Collins, K. A., et al. 2017, Natur, 546, 514
Ginzburg, S., & Sari, R. 2015, ApJ, 803, 111
Ginzburg, S., & Sari, R. 2017, MNRAS, 464, 3937
Ginzburg, S., Schlichting, H. E., & Sari, R. 2016, ApJ, 825, 29
Goldreich, P., & Nicholson, P. D. 1989, ApJ, 342, 1079
Goldreich, P., & Sari, R. 2003, ApJ, 585, 1024
Grannan, A. M., Favier, B., Le Bars, M., & Aurnou, J. M. 2017, GeoJI, 208, 1690
Guillot, T., Gautier, D., Chabrier, G., & Mosser, B. 1994, Icar, 112, 337
Guillot, T., & Showman, A. P. 2002, A&A, 385, 156
Harris, A. W. 1978, LPSCI, 9, 459
Howard, A. W., Marcy, G. W., Johnson, J. A., et al. 2010, Sci, 330, 653
Ida, & Ida, D. N. C. 2004, ApJ, 604, 388
Ikoma, M., Nakazawa, K., & Emori, H. 2000, ApJ, 537, 1013
Inamdar, N. K., & Schlichting, H. E. 2015, MNRAS, 448, 1751
Inamdar, N. K., & Schlichting, H. E. 2016, ApJL, 817, 13
Jackson, B., Arras, P., Penev, K., Peacock, S., & Marchant, P. 2017, ApJ, 835, 145
Jermyn, A. J., Tout, C. A., & Ogilvie, G. I. 2017, MNRAS, 469, 1768
Jia, S., & Spruit, H. C. 2017, MNRAS, 465, 149
Jin, S., & Mordasini, C. 2017, arXiv:170600251
Kippenhahn, R., Weigert, A., & Weiss, A. 2012, Stellar Structure and Evolution (Berlin: Springer)
Komacek, T. D., & Youdin, A. N. 2017, ApJ, 844, 94
Lambrechts, M., & Lega, E. 2017, A&A, 606, 146
Lecoanet, D., & Quataert, E. 2013, MNRAS, 430, 2363
Leconte, J., & Chabrier, G. 2012, A&A, 540, 20
Lee, E. J., & Chiang, E. 2015, ApJ, 811, 41
Lee, E. J., & Chiang, E. 2016, ApJ, 817, 90
Lee, E. J., Chiang, E., & Ormel, C. 2014, ApJ, 797, 95
Liu., S. F., Hori, Y., Lin, D. N. C., & Asphaug, E. 2015, ApJ, 812, 164
Long, M., Romanova, M. M., & Lovelace, R. V. E. 2005, ApJ, 634, 1214
Lopez, E. D., & Fortney, J. J. 2014, ApJ, 792, 1
Marleau, G. D., & Cumming, A. 2014, MNRAS, 437, 1378
Mizuno, H. 1980, PThPh, 64, 544
Mizuno, H., Nakazawa, K., & Hayashi, C. 1978, PThPh, 60, 699
Mordasini, C., Klahr, H., Alibert, Y., Miller, N., & Henning, T. 2014, A&A, 566, 141
Murray-Clay, R. A., Chiang, E. I., & Murray, N. 2009, ApJ, 693, 23
Ormel, C. W. 2014, ApJL, 789, L18
Owen, J. E., & Wu, Y. 2013, ApJ, 775, 105
Owen, J. E., & Wu, Y. 2017, ApJ, 847, 29
Perri, F., & Cameron 1974, Icar, 22, 416
Petigura, E. A., Marcy, G. W., & Howard, A. W. 2013, ApJ, 770, 69
Piso, A. M., & Youdin, A. N. 2014, ApJ, 786, 21
Pollack, J. B., Hubickyj, O., Bodenheimer, P., & Lissauer, J. 1996, Icar, 124, 62
Pu, B., & Valencia, D. 2017, ApJ, 846, 47
Rafikov, R. R. 2006, ApJ, 648, 666
Rogers, L. A., & Seager, S. 2010, ApJ, 716, 1208
Stevenson, D. J. 1982, P&SS, 30, 755
Stevenson, D. J. 1985, Icar, 62, 4
Tsang, D. 2011, ApJ, 741, 109
Valsecchi, F., Rappaport, S., Rasio, F. A., Marchant, P., & Rogers, L. A. 2015, ApJ, 813, 101
Weiss, L. M., & Marcy, G. W. 2014, ApJL, 783, L6
Wolfgan, A., & Lopez, E. 2015, ApJ, 806, 183
Wu, Y., & Lithwick, Y. 2013, ApJ, 772, 74
Youdin, A. N., & Mitchell, J. L. 2010, ApJ, 721, 1113
Yu, C., Li, H., Li, S. T., Lin, D. N. C., & Lubow, S. 2011, ApJ, 712, 198
Zahn, J. P. 1977, A&A, 57, 383